Generalized Thermo-poroelasticity Equations and Wave Simulation

Enjiang Wang[1,2] · José M. Carcione[3,4] · Fabio Cavallini[4] · Marco Botelho[5] · Jing Ba[3]

Abstract

We establish a generalization of the thermoelasticity wave equation to the porous case, including the Lord–Shulman (LS) and Green–Lindsay (GL) theories that involve a set of relaxation times (τ_i, $i = 1, \dots, 4$). The dynamical equations predict four propagation modes, namely, a fast P wave, a Biot slow wave, a thermal wave, and a shear wave. The plane-wave analysis shows that the GL theory predicts a higher attenuation of the fast P wave, and consequently a higher velocity dispersion than the LS theory if $\tau_1 = \tau_2 > \tau_3$, whereas both models predict the same anelasticity for $\tau_1 = \tau_2 = \tau_3$. We also propose a generalization of the LS theory by applying two different Maxwell–Vernotte–Cattaneo relaxation times related to the temperature increment (τ_3) and solid/fluid strain components (τ_4), respectively. The generalization predicts positive quality factors when $\tau_4 \geq \tau_3$, and increasing τ_4 further enhances the attenuation. The wavefields are computed with a direct meshing algorithm using the Fourier pseudospectral method to calculate the spatial derivatives and a first-order explicit Crank–Nicolson time-stepping method. The propagation illustrated with snapshots and waveforms at low and high frequencies is in agreement with the dispersion analysis. The study can be useful for a comprehensive understanding of wave propagation in high-temperature high-pressure fields.

Keywords Thermoelasticity · Poroelasticity · Waves · Simulation · Fourier pseudospectral method

---

✉ Jing Ba
  jingba@188.com

1   Key Lab of Submarine Geosciences and Prospecting Techniques, MOE, College of Marine Geosciences, Ocean University of China, Qingdao 266100, China

2   Evaluation and Detection Technology Laboratory of Marine Mineral Resources, Qingdao National Laboratory for Marine Science and Technology, Qingdao 266061, China

3   School of Earth Sciences and Engineering, Hohai University, Nanjing 211100, China

4   Istituto Nazionale di Oceanografia e di Geofisica Sperimentale (OGS), Borgo Grotta Gigante 42c, 34010 Sgonico, Trieste, Italy

5   Instituto de Geociencias/CPGG, Campus Universitario de Ondina, Universidade Federal da Bahia, 40170-110 Salvador, BA, Brasil

1 Introduction

The theory of thermo-poroelasticity describes the coupling between the fields of deformation and temperature. Specifically, an elastic source gives rise to a temperature field and attenuation, whereas a heat source induces anelastic deformations. This theory is useful for a variety of fields such as seismic attenuation (Budiansky et al. 1983; Armstrong 1984), geothermal exploration (Rawal and Ghassemi 2014; Jacquey et al. 2015; Poletto et al. 2018), and thermodynamics (Berezovski and Maugin 2001). Detailed reviews on thermoelasticity can be found in Ignaczak and Ostoja-Starzewski (2010).

Biot (1956) derived the classical parabolic-type differential equations for the Fourier law of heat conduction. However, this theory has unphysical solutions as a function of frequency, such as discontinuities and infinite velocities. Lord and Shulman (1967) formulated a more physical system of equations by introducing a single relaxation term into the hyperbolic-type heat equation. This theory leads to an attenuation kernel by analogy with the Maxwell model of viscoelasticity, and predicts a wave-like propagation behavior at high frequencies (Carcione et al. 2019b). A generalization of this theory to the anisotropic case was studied by Dhaliwal and Sherief (1980). Green and Lindsay (1972) derived an alternative theory by introducing two different relaxation times into the constitutive relations for the stress tensor and the entropy to represent the dependence of elasticity on temperature rate. A comprehensive review of the research works on thermoelasticity is given by Hetnarski and Ignaczak (1999). These two theories predict two P waves and an S wave. The two P waves are an elastic wave and a thermal wave having similar characteristics to the fast and slow P waves of poroelasticity (Biot 1962). The S wave is not affected by the thermal effects (in homogeneous media). Rudgers (1990) studied the propagation speeds and absorption coefficients of these waves as a function of frequency. More recently, Carcione et al. (2019b) developed a numerical algorithm for simulation of wave propagation in linear thermoelastic media, based on the theory of Lord and Shulman (1967). The algorithm is a grid method based on the Fourier differential operator and an explicit Crank–Nicolson time-integration method. Wang et al. (2020) derived the frequency-domain Green function of the Lord–Shulman (LS) thermoelasticity theory. Until now, the simulation of wave propagation in thermoelastic media on the basis of the Green and Lindsay (GL) theory still has not been achieved.

Poroelastic attenuation, due to conversion of the fast P wave to the slow mode, is analogous to the thermoelastic loss (Norris 1992; Carcione et al. 2020). Biot (1962) first considered a matrix (skeleton or frame) fully saturated with a fluid and formulated the theory of dynamic poroelasticity. This theory predicts the existence of two compressional (P) waves and a shear wave. The second slow P wave is diffusive at low frequencies and wave-like at high frequencies. The theory makes no assumption on the shape and geometry of the pores and grains, and pioneers the study of wave propagation in porous media. The Biot theory was verified extensively by a large number of experimental studies (Berryman 1981; Kelder and Smeulders 1997; Gurevich et al. 1999).

The theory of porothermoelasticity combines the equation of heat conduction with the poroelasticity equations to describe the couplings between the stress components and temperature fields in porous media (Bear et al. 1992; Sharma 2008). Youssef (2007) derived the governing equations that describe the behavior of thermoelastic porous media in the context of a generalized thermoelasticity with one relaxation time (LS), and further proved the uniqueness of the solution. On the basis of this theory, Singh (2011) investigated the propagation of plane waves, and discussed the effect of porosity on the different waves. Sharma (2008)

studied the propagation and attenuation of the four waves, namely, a fast P wave, a slow Biot wave, a slow thermal wave, and a shear wave. The two slow waves present a diffusive behavior under certain conditions, depending on viscosity, frequency, and the thermoelastic constants. Carcione et al. (2019a) derived the thermo-poroelastic equations by combining Biot equations with those of Lord and Shulman (1967). The wavefields are computed with a meshing algorithm using the Fourier pseudospectral method.

In this work, we present a system of generalized thermo-poroelasticity equations. The equations comprise the LS and GL theories, depending on specific relaxation times. Moreover, we further discuss the generalization of the original LS theory, by varying the two Maxwell–Vernotte–Cattaneo relaxation times in the heat equation. The corresponding plane-wave analysis is carried out, which shows the differences (velocity and attenuation) between the LS and GL theories. We then develop a numerical algorithm for the simulations of wave propagation. The algorithm, based on a direct-grid method, computes snapshots and waveforms that illustrate wave propagation in general thermo-poroelastic media.

2 Equations of Motion

Considering a 2D isotropic medium, let us define by v_i and q_i, $i = x, z$, the components of the particle velocities of the frame and fluid relative to the frame, respectively, σ_{ij} the components of the total stress tensor, p the fluid pressure, and T the increment of temperature above a reference absolute temperature T_0 corresponding to the state of zero stress and strain. The general dynamic thermo-poroelasticity equations, including both the LS and GL models, can be obtained with a modification of the equations given in Carcione et al. (2019a) as follows.

Constitutive equations:

$$
\begin{aligned}
\dot{\sigma}_{xx} &= 2\mu v_{x,x} + \lambda \epsilon_m + \alpha M \epsilon - \beta(\dot{T} + \tau_1 \ddot{T}) + f_{xx}, \\
\dot{\sigma}_{zz} &= 2\mu v_{z,z} + \lambda \epsilon_m + \alpha M \epsilon - \beta(\dot{T} + \tau_1 \ddot{T}) + f_{zz}, \\
\dot{\sigma}_{xz} &= \mu(v_{x,z} + v_{z,x}) + f_{xz}, \\
\dot{\sigma}_f &= -\phi \dot{p} = \phi M \epsilon - \beta_f(\dot{T} + \tau_2 \ddot{T}) + f_f, \\
\epsilon &= \alpha \epsilon_m + \epsilon_f, \quad \epsilon_m = v_{x,x} + v_{z,z}, \quad \epsilon_f = q_{x,x} + q_{z,z},
\end{aligned}
\tag{1}
$$

where τ_1 and τ_2 are the relaxation times representing the dependence of elastic behavior on temperature rate, f_{xx}, f_{zz}, f_{xz} and f_f are the external sources, and β and β_f are the coefficients of thermoelasticity of the bulk material and fluid, respectively. The subscript ", i" denotes the spatial derivative and a dot above a variable indicates a time derivative. The subscripts "m" and "f" refer to the solid (dry) matrix and the fluid, respectively. λ is the Lamé constant of the dry rock, μ is the shear modulus of the dry (and saturated) rock, M is related to the elastic coupling between the solid and the fluid and α is Biot's effective stress coefficient. We have

$$
\begin{aligned}
M &= \frac{K_s}{1 - \phi - K_m/K_s + \phi K_s/K_f}, \\
\alpha &= 1 - \frac{K_m}{K_s}, \\
K_m &= \lambda + \frac{2}{3}\mu,
\end{aligned}
\tag{2}
$$

where ϕ is the porosity, and K_m, K_s and K_f the bulk moduli of the drained matrix, solid and fluid, respectively.

The corresponding dynamical equations are:

$$
\begin{aligned}
\sigma_{xx,x} + \sigma_{xz,z} &= \rho\dot{v}_x + \rho_f\dot{q}_x + f_x, \\
\sigma_{xz,x} + \sigma_{zz,z} &= \rho\dot{v}_z + \rho_f\dot{q}_z + f_z, \\
-p_{,x} &= \rho_f\dot{v}_x + m\dot{q}_x + \frac{\eta}{\kappa}q_x, \\
-p_{,z} &= \rho_f\dot{v}_z + m\dot{q}_z + \frac{\eta}{\kappa}q_z,
\end{aligned}
\tag{3}
$$

where

$$
\rho = (1 - \phi)\rho_s + \phi\rho_f
\tag{4}
$$

is the composite density, with ρ_s and ρ_f the solid and fluid densities, respectively. The parameter $m = \mathcal{T}\rho_f/\phi$, with $\mathcal{T}$ the tortuosity of pores, describes the inertial coupling between fluid and solid phases, η is the fluid viscosity, κ is the permeability of the medium, and f_i are the external forces. The Darcy law defines the movement of the viscous fluid, which is assumed to be of a Poiseuille type at low frequencies.

The Fourier law of heat conduction is

$$
\Delta_\gamma T = c(\dot{T} + \tau_3\ddot{T}) + \beta T_0\left[(\epsilon_m + \tau_4\dot{\epsilon}_m) + (\epsilon_f + \tau_4\dot{\epsilon}_f)\right] + q,
\tag{5}
$$

where

$$
\Delta_\gamma = (\gamma T_{,x})_{,x} + (\gamma T_{,z})_{,z}
\tag{6}
$$

(Dhaliwal and Sherief 1980), with γ the bulk coefficient of heat conduction, and $\Delta_\gamma = \gamma\Delta$ in the homogeneous case with Δ the Laplacian; c is the bulk specific heat of the unit volume in the absence of deformation, τ_3 and τ_4 are Maxwell–Vernotte–Cattaneo relaxation times, respectively, q is the heat source.

These equations assume thermal equilibrium between the solid and fluid, i.e., the temperature in both phases is the same. Thermal equilibrium is valid when the interstitial heat transfer coefficient between the solid and fluid is very large and the ratio of pore surface area to pore volume is sufficiently high. Equations (1), (3) and (5) include both the GL and the LS models. The first is obtained with $\tau_4 = 0$, whereas the second with $\tau_1 = \tau_2 = 0$ and $\tau_3 = \tau_4 \equiv \tau$, in which case, the equations are those of Carcione et al. (2019a). Ignaczak and Ostoja-Starzewski (2010, p. 23) show that the GL relaxation times must satisfy $\tau_1 = \tau_2 \geq \tau_3$ [their Eq. (1.3.56)]. Moreover, in the case $\tau_1 = \tau_2 = \tau_3$, the so-called central operators of the LS and GL theories coincide (Corollary 6.1 of Ignaczak and Ostoja-Starzewski 2010, p. 132), although this does not mean that the temperature in both theories is the same.

3 Particle Velocity–Stress–Temperature Formulation

Following Carcione et al. (2019a), in the following, we recast Eqs. (1), (3) and (5) as new expressions to be used for the numerical simulation of the fields.

Equations (3) yield

$$\dot{v}_x = \beta_{11}(\sigma_{xx,x} + \sigma_{xz,z} - f_x) - \beta_{12}\left(p_{,x} + \frac{\eta}{\kappa}q_x\right) \equiv \Pi_x,$$
$$\dot{v}_z = \beta_{11}(\sigma_{xz,x} + \sigma_{zz,z} - f_z) - \beta_{12}\left(p_{,z} + \frac{\eta}{\kappa}q_z\right) \equiv \Pi_z,$$
$$\dot{q}_x = \beta_{21}(\sigma_{xx,x} + \sigma_{xz,z} - f_x) - \beta_{22}\left(p_{,x} + \frac{\eta}{\kappa}q_x\right) \equiv \Omega_x,$$
$$\dot{q}_z = \beta_{21}(\sigma_{xz,x} + \sigma_{zz,z} - f_z) - \beta_{22}\left(p_{,z} + \frac{\eta}{\kappa}q_z\right) \equiv \Omega_z,$$

$$(7)$$

where

$$\begin{bmatrix} \beta_{11} & \beta_{12} \\ \beta_{21} & \beta_{22} \end{bmatrix} = (\rho_f{}^2 - \rho m)^{-1} \begin{bmatrix} -m & \rho_f \\ \rho_f & -\rho \end{bmatrix}. \tag{8}$$

Defining

$$\dot{T} = \psi, \tag{9}$$

Eq. (5) becomes

$$\dot{\psi} = (c\tau_3)^{-1}\left[\Delta_\gamma T - q - \beta T_0(\epsilon_m + \tau_4(\Pi_{x,x} + \Pi_{z,z}) + \epsilon_f + \tau_4(\Omega_{x,x} + \Omega_{z,z}))\right] - \frac{1}{\tau_3}\psi \equiv \Pi. \tag{10}$$

The velocity–stress–temperature system of equations is completed with the constitutive equations in (1), which can be re-written as

$$\dot{\sigma}_{xx} = 2\mu v_{x,x} + \lambda\epsilon_m + \alpha M\epsilon - \beta(\psi + \tau_1\Pi) + f_{xx},$$
$$\dot{\sigma}_{zz} = 2\mu v_{z,z} + \lambda\epsilon_m + \alpha M\epsilon - \beta(\psi + \tau_1\Pi) + f_{zz}. \tag{11}$$
$$\dot{\sigma}_f = -\phi\dot{p} = \phi M\epsilon - \beta_f(\psi + \tau_2\Pi) + f_f.$$

A plane-wave analysis to obtain the phase velocity and attenuation factor of the wave modes is given in Appendix 1. The equations predict three P waves, namely, a fast P wave, a Biot slow wave and a slow thermal wave.

3.1 The Algorithms

The velocity–stress–temperature differential equations can be written in matrix form as

$$\dot{\mathbf{v}} + \mathbf{s} = \mathbf{M}\mathbf{v}, \tag{12}$$

where

$$\mathbf{v} = [v_x, v_z, q_x, q_z, \sigma_{xx}, \sigma_{zz}, \sigma_{xz}, p, T, \psi]^\top \tag{13}$$

is the unknown array vector,

$$\mathbf{s} = [-\beta_{11}f_x, -\beta_{11}f_z, -\beta_{21}f_x, -\beta_{21}f_z, f_{xx}, f_{zz}, f_{xz}, -f_f/\phi, 0, q']^\top \tag{14}$$

is the source vector with $q' = -(c\tau_3)^{-1}q$, and $\mathbf{M}$ is the propagation matrix containing the spatial derivatives and medium properties. Following Carcione et al. (2019a), the solution to equation (12) subject to the initial condition $\mathbf{v}(0) = \mathbf{v}_0$ is

$$\mathbf{v}(t) = \exp(t\mathbf{M})\mathbf{v}_0 + \int_0^t \exp(\tau\mathbf{M})\mathbf{s}(t - \tau)\mathrm{d}\tau, \qquad (15)$$

where $\exp(t\mathbf{M})$ is the evolution operator.

The eigenvalues of $\mathbf{M}$ have negative real parts and differ greatly in magnitude. The presence of large eigenvalues, together with small eigenvalues, makes the problem stiff (Carcione et al. 2019a), and the real positive eigenvalues can induce instability during the computation. We solve the stiff problems with the Crank–Nicolson time-integration methods given in Appendix 2. The spatial derivatives are calculated with the Fourier method by using the FFT. This spatial approximation is infinitely accurate for band-limited periodic functions with cutoff spatial wavenumbers which are smaller than the cutoff wavenumbers of the mesh. Alternatively, another time stepping method based on a second-order accurate splitting or partition method can be used. This method solves both problems (stiffness and instability) by calculating the unstable part of the differential equations analytically. The method for the LS model has been implemented in Carcione et al. (2019a, Appendix C).

4 Physics and Simulations

We consider the medium properties given in Table 1. The coefficients of thermal expansion α_m and α_f are 2.715×10^{-6} °K^{-1} and 3.333×10^{-5} °K^{-1}, respectively, such that $\beta_m = 3\alpha_m K_s$ = 3.91×10^5 kg/(m s^2 °K), and $\beta_f = 3\alpha_f K_f = 2.2 \times 10^5$ kg/(m s^2 °K) (Sharma 2008). Here we use a large γ for a better illustration of the physics. On the basis of properties given in Table 1, we compare the LS and GL theories, with a plane-wave analysis and wavefield simulations, and illustrate the results of a generalized LS theory.

Table 1 Medium properties

Grain bulk modulus, K_s	48 GPa
Density, ρ_s	2650 kg/m^3
Frame bulk modulus, K_m	2.4 GPa
Shear modulus, μ_m	3 GPa
Porosity, ϕ	0.3
Permeability, κ	1 darcy
Tortuosity, $\mathcal{T}$	2
Water density, ρ_f	1000 kg/m^3
Viscosity, η_f	0.001 Pa s
Bulk modulus, K_f	2.2 GPa
Thermoelasticity coefficient, β_f	2.2×10^5 kg/(m s^2 °K)
Bulk specific heat, c	3×10^5 kg/(m s^2 °K)
Thermoelasticity coefficient, β	6×10^5 kg/(m s^2 °K)
Absolute temperature T_0	300 °K
Thermal conductivity, γ	1.4×10^7 m kg/(s^3 °K)
Relaxation time, τ_1	3×10^{-3} s
Relaxation time, τ_2	3×10^{-3} s
Relaxation time, τ_3	1.5×10^{-3} s
Relaxation time, τ_4	1.5×10^{-3} s

4.1 Comparison Between the Lord–Shulman and Green–Lindsay Theories

As has been discussed in Ignaczak and Ostoja-Starzewski (2010), the relaxation times of the GL model satisfy $\tau_1 = \tau_2 \geq \tau_3$. If $\tau_1 = \tau_2 = \tau_3$, the so-called central operators of the LS and GL theories coincide. Figures 1 and 2 show the phase velocities and dissipation factors of the fast P-wave, slow P-wave and T-wave as a function of frequency when $\tau_1 = \tau_2 > \tau_3$, and $c = 3 \times 10^5$ kg/(m s^2 °K). We observe that the slow and thermal waves are strongly diffusive at low frequencies. The fast P wave has two relaxation peaks at 100 Hz and 20 kHz, respectively, corresponding to the thermal loss and Biot mechanism. The GL theory exhibits more thermal loss than the LS theory, and consequently has a larger velocity dispersion, and predicts a higher velocity at the high frequencies. The T-wave and slow P-wave are wave-like at high frequencies. At these frequencies, the GL theory predicts a slightly higher slow P-wave phase velocity but a smaller T-wave velocity than the LS theory.

A smaller value of $c = 3 \times 10^4$ kg/(m s^2 °K) highlights the difference between the two theories. As displayed in Figs. 3 and 4, decreasing c induces a much higher attenuation of the fast P-wave, and enhances the velocity dispersion, especially for the GL theory. The slow P-wave and T-wave velocity differences at high frequencies between the two theories become more evident. The thermal wave has another relaxation peak at 10 kHz, and consequently exhibits another velocity dispersion at high frequencies. A smaller c yields larger propagation velocities of the fast P-wave, slow P-wave and T-wave at high frequencies. It is evident that the waves propagate with different characteristics at different frequencies,
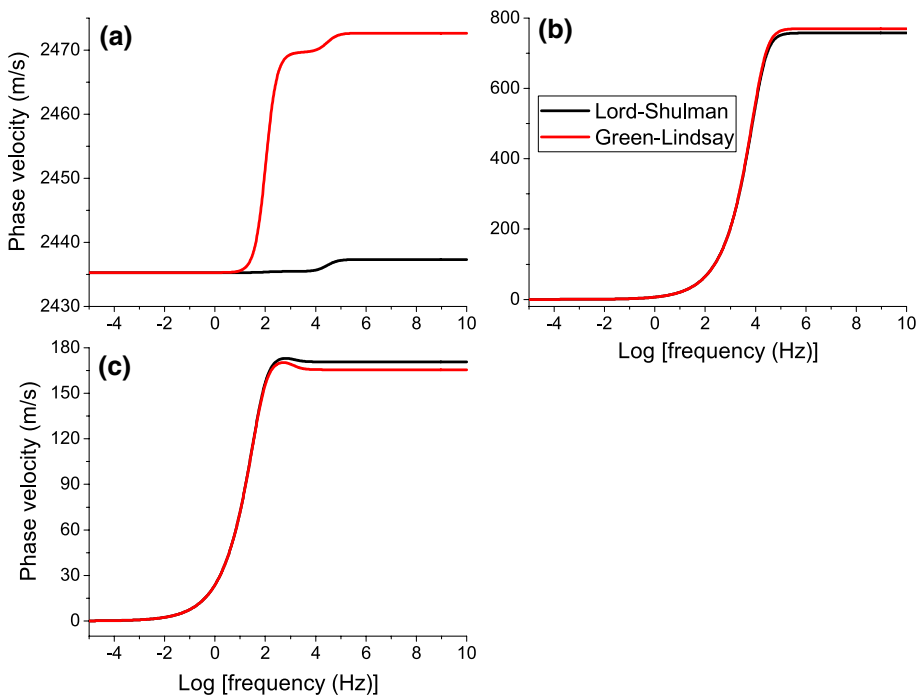

Fig. 1 Phase velocities of the **a** fast P-wave, **b** slow P-wave, and **c** the T-wave, as a function of frequency. $c = 3 \times 10^5$ kg/(m s^2 °K). The LS results are obtained by using $\tau_1 = \tau_2 = 0$, and $\tau_3 = \tau_4 = 1.5 \times 10^{-3}$ s, whereas the GL results are obtained with $\tau_1 = \tau_2 = 3 \times 10^{-3}$ s, $\tau_3 = 1.5 \times 10^{-3}$ s, and $\tau_4 = 0$
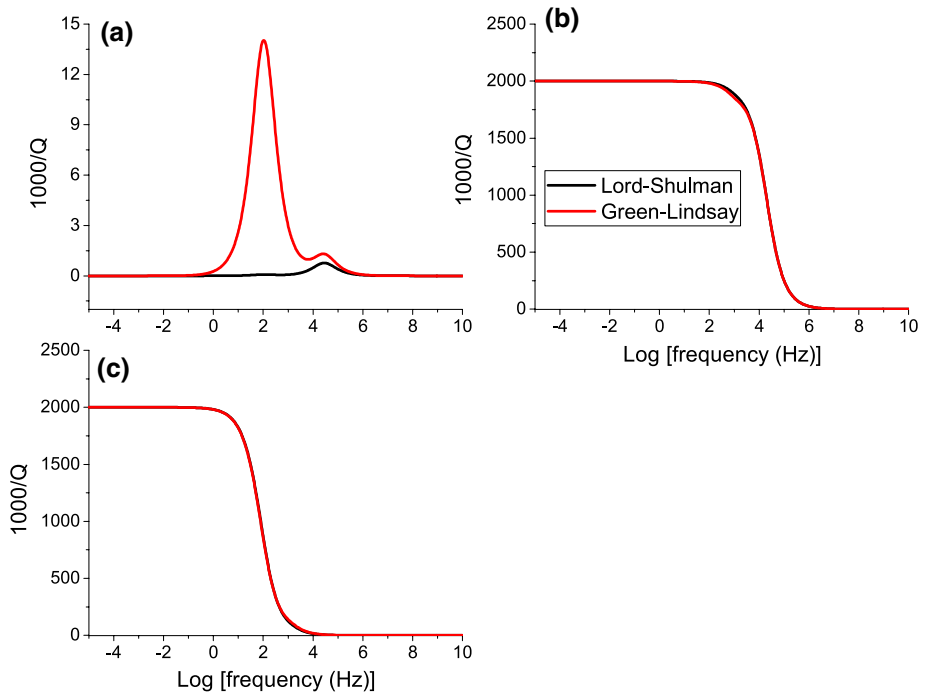
Fig. 2 Dissipation factors of the **a** fast P-wave, **b** slow P-wave, and **c** the T-wave, corresponding to Fig. 1

which is illustrated in the following numerical examples. Moreover, the curves indicated with circles, showing the results of the GL model when $\tau_1 = \tau_2 = \tau_3$, overlap with those of the LS theory, confirming that both theories coincide in this case, as has been theoretically shown by Ignaczak and Ostoja-Starzewski (2010).

In the following, we use the smaller value of c in Figs. 3 and 4 to highlight the T-wave propagation, and simulate the wavefields using the algorithm given in Appendix 2. We consider a model with 232×232 grid points. The source is located at the center of the model and its time history is

$$h(t) = \cos[2\pi(t - t_0)f_0]\exp\left[-2(t - t_0)^2 f_0^2\right], \tag{16}$$

where f_0 is the central frequency and $t_0 = 3/(2f_0)$ is the time delay.

We first consider a central frequency of 500 Hz, where the T-wave and slow wave have wave-like and diffusive behaviors, respectively. We assume a grid spacing of $dx = dz = 0.3$ m and a time step $dt = 0.015$ ms. The sources are dilatational (f_{xx}, f_{zz}, and f_f) to highlight only the compressional waves. Figures 5, 6 and 7 show the simulated snapshots of v_z, q_z and T at 14.25 ms, respectively.

We observe that the fast P-wave computed with the LS theory propagates more slowly but exhibits smaller attenuation than that predicted by the GL theory. The slow P-wave is diffusive due to the strong attenuation and the wavefront is confined to the source location in the q_z snapshot. The T wave is more attenuated than the fast P wave and can be seen in the inner wavefront, particularly in the T-component snapshot. The GL theory predicts a smaller T-wave phase velocity than the LS theory. All
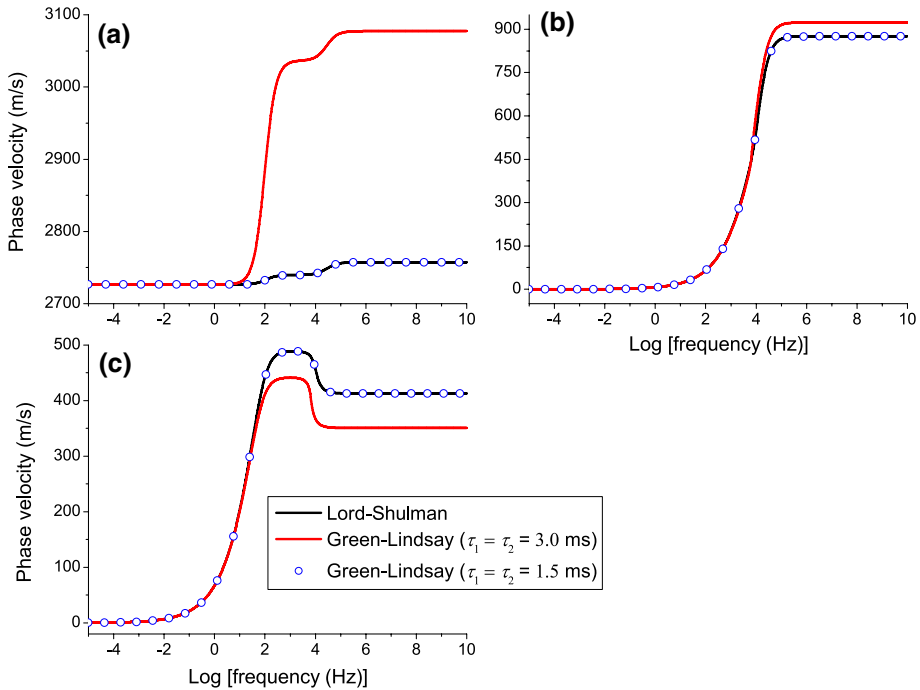
Fig. 3 Phase velocities of the **a** fast P-wave, **b** slow P-wave, and **c** the T-wave, as a function of frequency. $c = 3 \times 10^4$ kg/(m s^2 °K). The LS results are obtained by using $\tau_1 = \tau_2 = 0$, and $\tau_3 = \tau_4 = 1.5 \times 10^{-3}$ s. The GL results in red lines are obtained with $\tau_1 = \tau_2 = 3 \times 10^{-3}$ s, $\tau_3 = 1.5 \times 10^{-3}$ s, and $\tau_4 = 0$, whereas those represented by the blue circles, which overlap with the black lines, are obtained with $\tau_1 = \tau_2 = 1.5 \times 10^{-3}$ s, $\tau_3 = 1.5 \times 10^{-3}$ s, and $\tau_4 = 0$

these conclusions are in agreement with the dispersion analysis shown in Figures 3 and 4. The corresponding waveforms of the v_z particle velocity at (24, 24) m are displayed in Fig. 8, which further confirms the above analyses. A comparison between the Crank–Nicolson and splitting schemes (Carcione et al. 2019a) for the LS model shows that both methods yield the same waveform, constituting a test with two different software codes, which confirms the effectiveness of the Crank–Nicolson scheme.

Next, we consider a central frequency of 1 MHz. A grid spacing of $dx = dz = 0.15$ mm, and $dt = 0.0075$ μs are used, and the sources are dilatational. Figures 9, 10 and 11 show the v_z, q_z and T snapshots at 7.125 μs, and Fig. 12 displays the waveform of the v_z-component at (13.5, 13.5) mm. Unlike those shown in Figs. 5, 6 and 7, all the three modes are wavelike, in agreement with the dispersion analysis of Figs. 3 and 4. The propagation differences are induced by the thermal and Biot losses, causing significant velocity dispersion and attenuation of the slow P and T waves when the frequency is increased from 500 Hz to 1 MHz (see Figs. 3 and 4). The fast P-wave velocity obtained with the GL theory is higher than that of the LS theory. On the contrary, the velocity of the T wave, based on the GL theory, is smaller. The waveforms in Fig. 12 further show these properties.
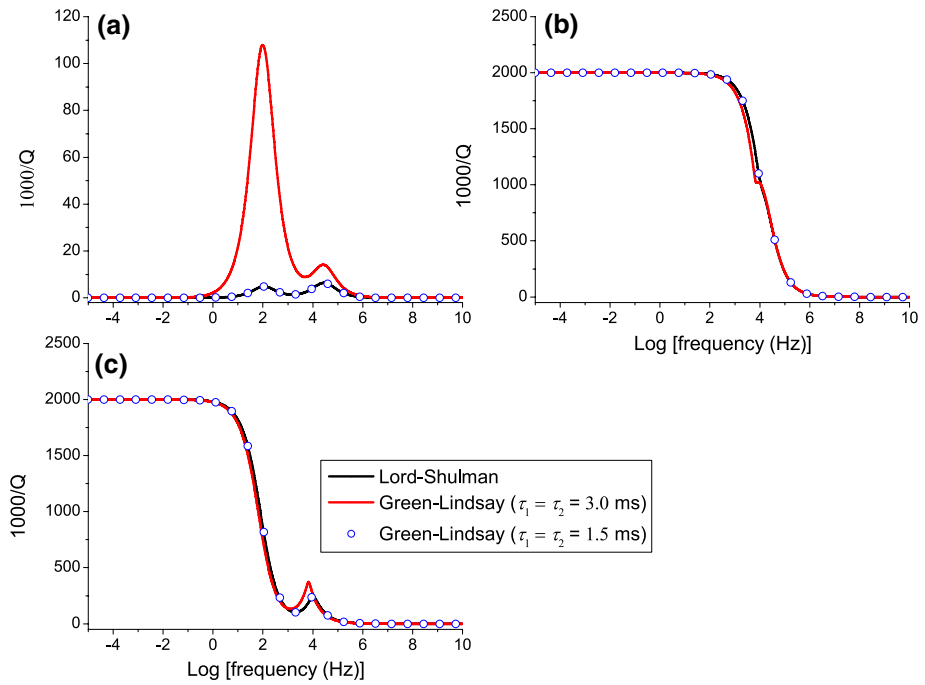
Fig. 4 Dissipation factors of **a** fast P-wave, **b** slow P-wave, and **c** the T-wave, corresponding to Fig. 3
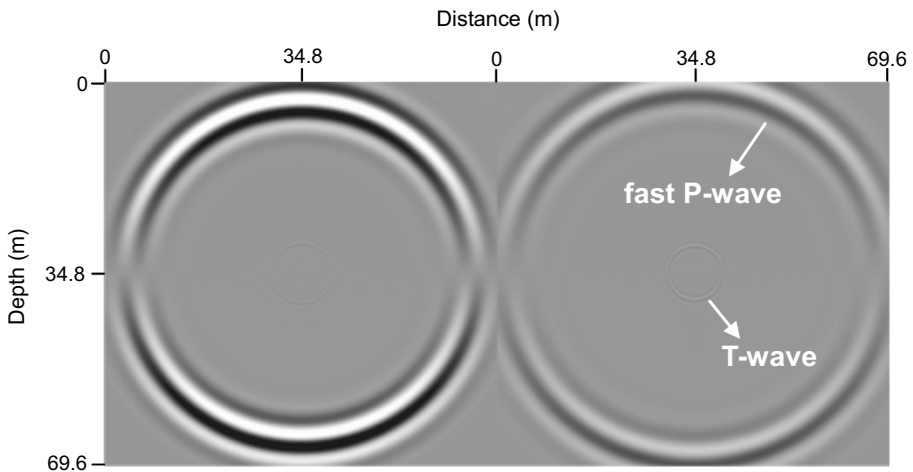

Fig. 5 Snapshots of the particle velocity of the frame v_z at 14.25 ms, based on the LS (left) and GL (right) theories, respectively. $c = 3 \times 10^4$ kg/(m s^2 °K). The dominant frequency of the source is 500 Hz

4.2 Generalized Lord–Shulman Theory

The original LS theory (Lord and Shulman 1967) assumes that the two relaxation times τ_3 and τ_4 are the same. The plane-wave analysis shows that $\tau_4 < \tau_3$, yields negative quality
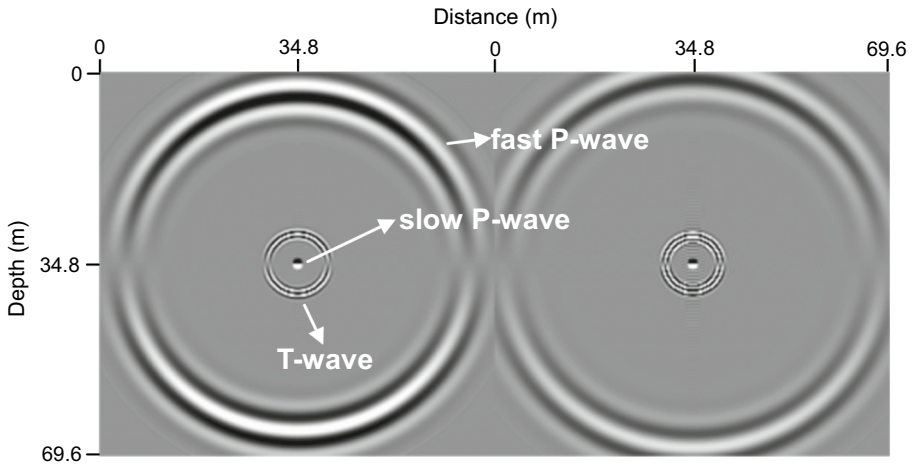
Fig. 6 Snapshots of the particle velocity of fluid relative to the solid q_z at 14.25 ms, corresponding to the LS (left) and GL (right) theories. $c = 3 \times 10^4$ kg/(m s^2 °K)

factors, indicating that the propagation is unstable. When $\tau_4 > \tau_3$, the quality factors are positive. In the following, we further examine this generalized LS theory by considering three different values of τ_4.

Figures 13 and 14 show the phase velocities and dissipation factors as a function of frequency, obtained with the generalized LS theory with different values of τ_4. In this case, $c = 3 \times 10^4$ kg/(m s^2 °K). We observe that the attenuation of the fast wave increases with increasing τ_4, which causes an increased velocity dispersion. At high frequencies, the phase velocities of the fast and slow waves increase with τ_4, whereas the T-wave velocity decreases.

Figures 15, 16 and 17 show the snapshots of v_z, q_z and T at 14.25 ms, using three values of τ_4. The modeling parameters are the same as those described in Figs. 5 and 6. Both the fast P- and T- wavefronts can be observed. Increasing τ_4, the velocity and attenuation of the fast P-wave increase. This can clearly be seen in Fig. 18, which shows the v_z waveform at (24, 24) m. The T-wave velocity decreases with increasing τ_4, and is more attenuated in comparison with the fast P wave, which is also in agreement with the dispersion analysis. The slow P-wave is diffusive and can be seen in the q_z snapshot at the source location.

Figures 19 and 20 show the simulated snapshots using a central frequency of 1 MHz. In this case, all three compressional wave modes are present. The velocities of the fast and slow waves increase with increasing τ_4, whereas those of the T-wave decrease. The waveforms displayed in Fig. 21 further prove this, in agreement with the plane-wave analysis. The slow wave and T wave can more clearly be observed in the q_z-component snapshot.

4.3 Heterogeneous Medium

Finally, we present a two-layer model. The upper medium has $K_m = 2.4$ GPa and $\mu_m = 3$ GPa, whereas the lower medium has $K_m = 9$ GPa and $\mu_m = 10$ GPa. Moreover, we take $c = 3 \times 10^4$ kg/(m s^2 °K) for the upper medium and $c = 6 \times 10^4$ kg/(m s^2 °K) for the lower medium. All the other properties are the same as those of Table 1.
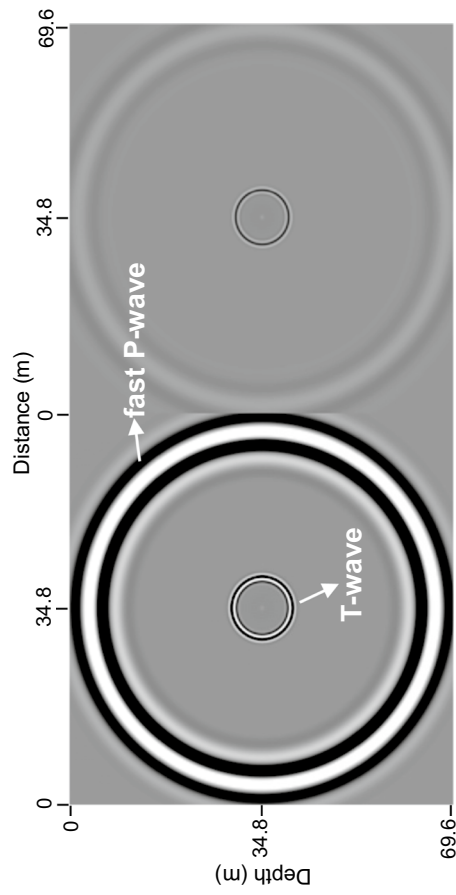
Fig. 7 Snapshots of the temperature wavefield T at 14.25 ms, corresponding to the LS (left) and GL (right) theories. $c = 3$ $\times 10^4$ kg/(m s^2 °K)

Fig. 8 Waveform comparison of the particle velocity of the frame v_z at (24, 24) m, corresponding to the LS (black line) and GL (red line) theories. $c = 3 \times 10^4$ kg/(m s² °K). The fields are normalized. The curve indicated with the circles, overlapping with the black curve, is obtained by using the time-splitting operator developed by Carcione et al. (2019a)
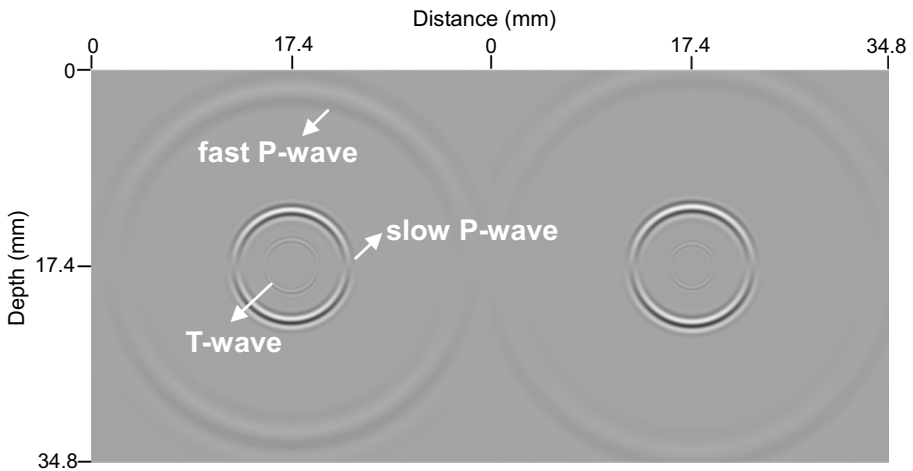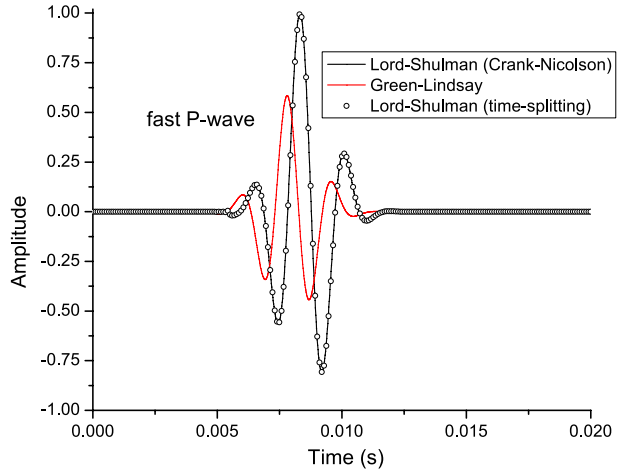
Fig. 9 Snapshots of the particle velocity of the frame v_z at 7.125 μs, corresponding to the LS (left) and GL (right) theories. $c = 3 \times 10^4$ kg/(m s² °K). The dominant frequency of the source is 1 MHz

Figure 22 shows the snapshots of the particle velocity of the fluid relative to the solid q_z, when the dominant frequency of the source is 500 Hz. The source is located at the center of the interface. We consider a 402×402 mesh, with $d_x = d_z = 0.3$ m, and a vertical source (f_z) is used, which also generates shear wave. As previously discussed, the slow wave is dissipative and can be recognized at the source location. In this case, the propagation of the S-wave is not affected by the thermal effect and therefore exhibits the same behavior when comparing the results of the LS and GL theories. On the contrary, the fast waves in the two layers are evidently affected, with the GL theory giving higher velocity and attenuation. The T-wave is more attenuated and can be seen in the inner wavefronts. Head (lateral) waves having a planar wavefront can also be observed.

Figures 23 and 24 show the snapshots of v_z and T, when the dominant frequency is 1 MHz. In this case, we consider a 402×402 mesh, with $d_x = d_z = 0.15$ mm. The
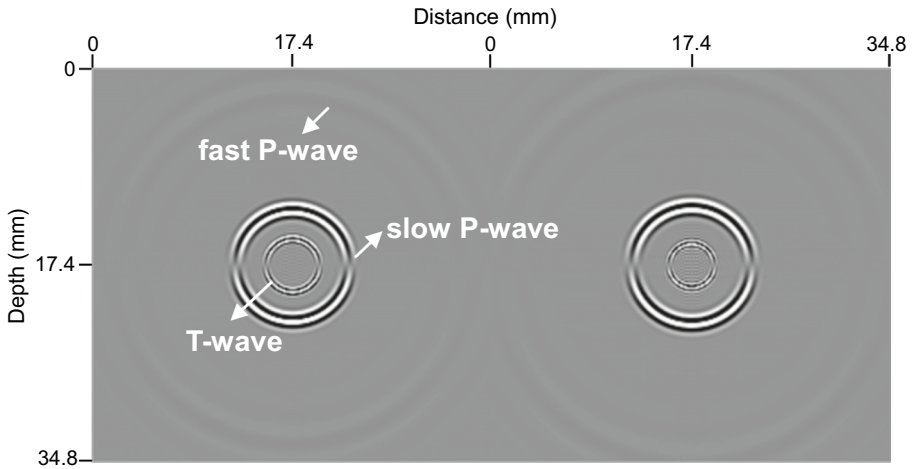
Fig. 10 Snapshots of the particle velocity of the fluid relative to the solid q_z at 7.125 μs, corresponding to the LS (left) and GL (right) theories. The dominant frequency of the source is 1 MHz
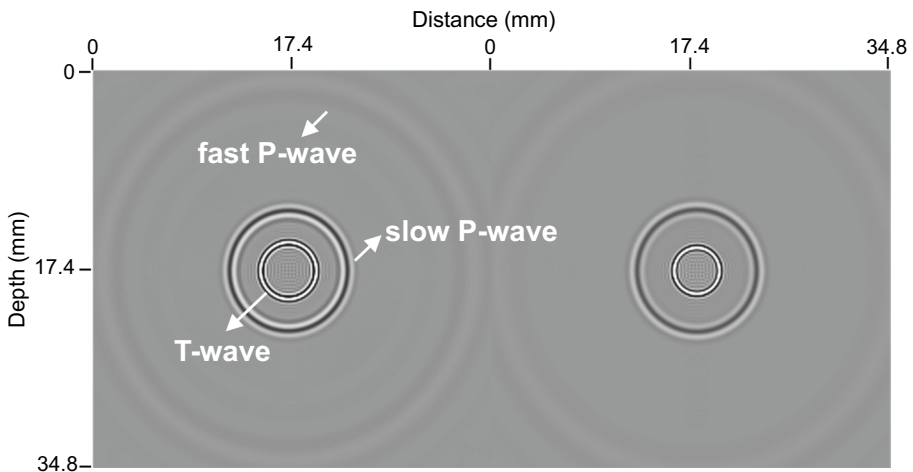

Fig. 11 Snapshots of the temperature wavefield T at 7.125 μs, corresponding to the LS (left) and GL (right) theories. The dominant frequency of the source is 1 MHz. The GL result has been enhanced by a factor 10^4

Biot slow wave propagates. The T-wave, which can be clearly identified as the inner wavefront in the T-component snapshot, propagates slower and is more attenuated in the lower medium, because a larger c is assumed. The shear wave is not present in the T-component snapshot. Even if the heterogeneity is simple, the wavefield can be complex. Substantial mode conversion occurs in more general media, making the interpretation of the wavefields more difficult.

Fig. 12 Waveform comparison at (13.5, 13.5) mm, between the LS (black line) and GL (red line) theories. $c = 3 \times 10^4$ kg/(m s^2 °K)
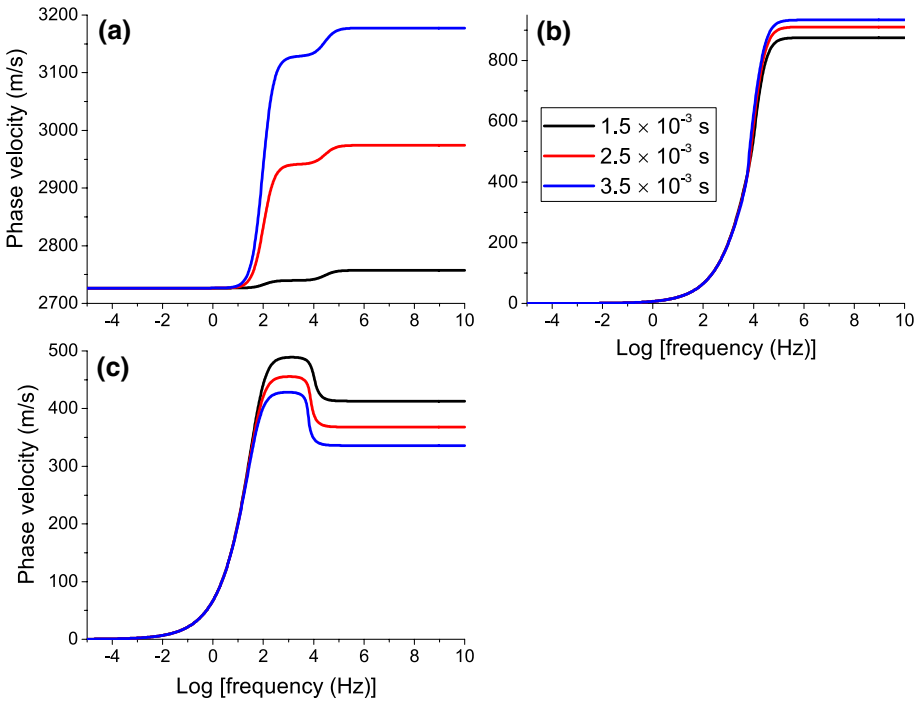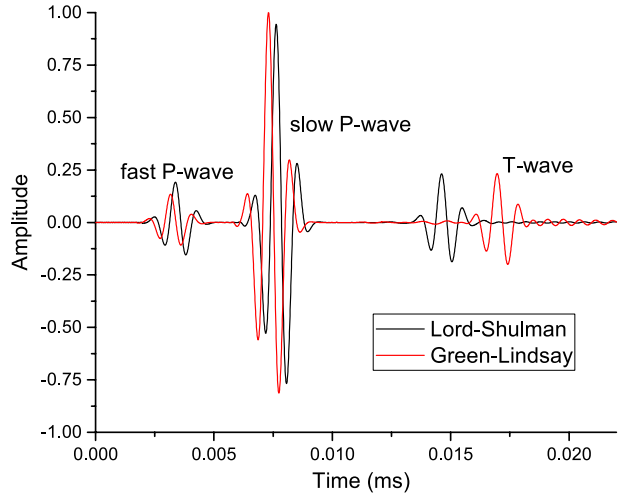

Fig. 13 Phase velocities of the **a** fast P-wave, **b** slow P-wave, and **c** the T-wave as a function of frequency, corresponding to the generalized LS theory with three different values of τ_4. $c = 3 \times 10^4$ kg/(m s^2 °K)

5 Conclusions

We have considered a generalized system of thermo-poroelasticity equations, which include the Lord–Shulman and Green–Lindsay theories. Moreover, we propose a numerical algorithm
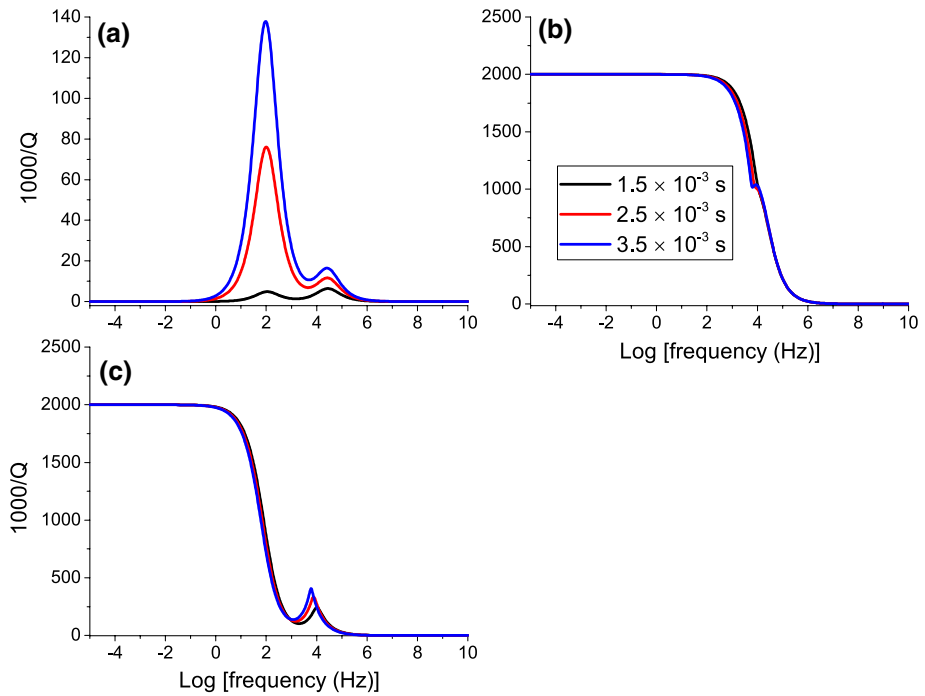
Fig. 14 Dissipation factors of the **a** fast P-wave, **b** slow P-wave, and **c** the T-wave, corresponding to Fig. 13
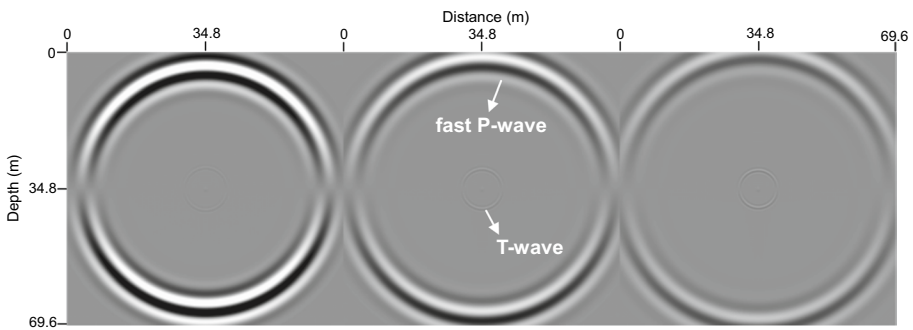

Fig. 15 Snapshots of the particle velocity of the frame v_z at 14.25 ms, corresponding to the generalized LS theories with $\tau_4 = 1.5 \times 10^{-3}$ s (left), 2.5×10^{-3} s (middle), and 3.5×10^{-3} s (right). $c = 3.0 \times 10^4$ kg/(m s^2 °K). The dominant frequency of the source is 500 Hz

to solve these equations. The dispersion analysis indicates that both theories predict four wave modes, namely, fast P wave, S wave, Biot slow wave and a thermal wave. The latter two are diffusive at low frequencies and wave-like at high frequencies. The Green–Lindsay theory predicts a higher attenuation and more velocity dispersion of the fast P-wave than the Lord–Shulman theory if $\tau_1 = \tau_2 > \tau_3$. The two theories coincide if $\tau_1 = \tau_2 = \tau_3$. The classic Lord–Shulman model can be further generalized by using two different values of the
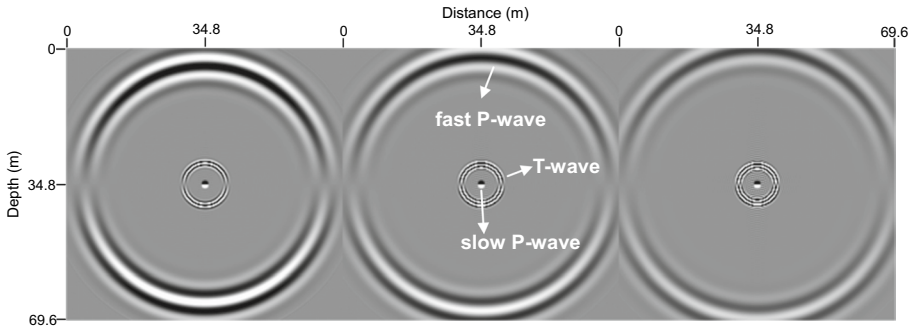
Fig. 16 Snapshots of the particle velocity of fluid relative to the solid q_z at 14.25 ms, corresponding to the generalized LS theory with $\tau_4 = 1.5 \times 10^{-3}$ s (left), 2.5×10^{-3} s (middle), and 3.5×10^{-3} s (right), respectively. $c = 3 \times 10^4$ kg/(m s^2 °K)
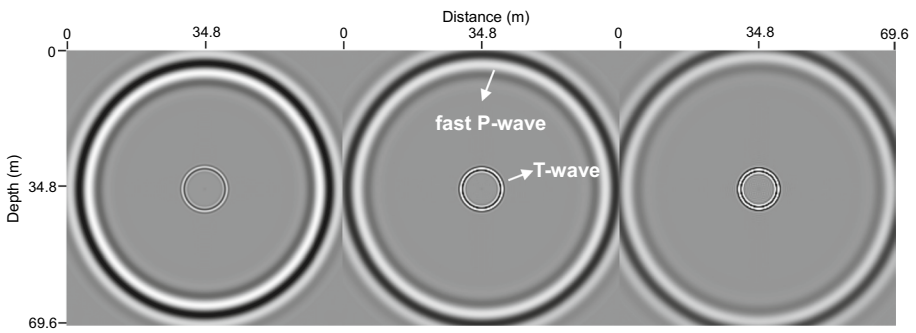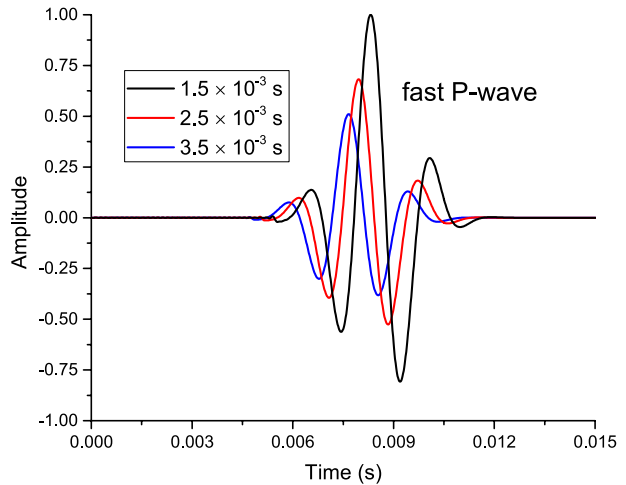

Fig. 17 Snapshots of the temperature wavefield T at 14.25 ms, corresponding to the generalized LS theory with $\tau_4 = 1.5 \times 10^{-3}$ s (left), 2.5×10^{-3} s (middle), and 3.5×10^{-3} s (right), respectively. $c = 3 \times 10^4$ kg/(m s^2 °K)

Fig. 18 Waveform comparison at (24, 24) m, corresponding to the generalized LS theory with three different values of τ_4. $c = 3 \times 10^4$ kg/(m s^2 °K)
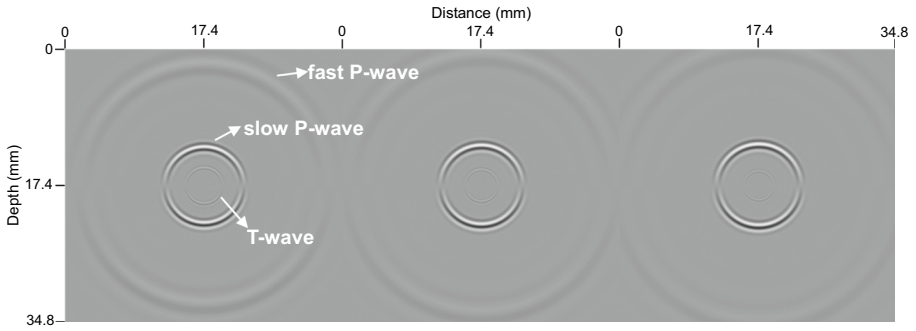
Fig. 19 Snapshots of the particle velocity of the frame v_z at 7.125 μs, corresponding to the generalized LS theory with $\tau_4 = 1.5 \times 10^{-3}$ s (left), 2.5×10^{-3} s (middle), and 3.5×10^{-3} s (right). $c = 3 \times 10^4$ kg/(m s^2 °K). The dominant frequency of the source is 1 MHz
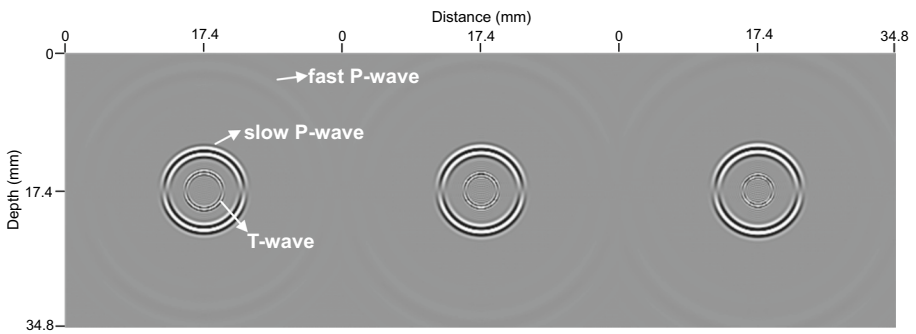

Fig. 20 Snapshots of the particle velocity of the fluid relative to the solid q_z at 7.125 μs, corresponding to the generalized LS theory, with $\tau_4 = 1.5 \times 10^{-3}$ s (left), 2.5×10^{-3} s (middle), and 3.5×10^{-3} s (right). $c = 3 \times 10^4$ kg/(m s^2 °K)

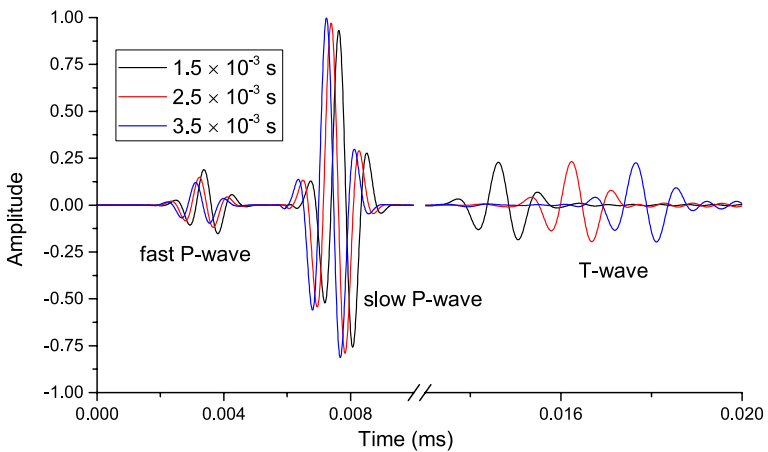**Fig. 21** Waveform comparison at (13.5, 13.5) mm, corresponding to the generalized LS theory, with three values of τ_4. $c = 3 \times 10^4$ kg/(m s^2 °K)

Fig. 22 Snapshots of the q_z component at 19.5 ms corresponding to the two-layer model, based on the LS (left) and GL (right) theories. The interface is located at a depth of 51 m. The differences between the upper and lower media are the values of the dry-rock moduli K_m, μ_m and the bulk specific heat c. The dominant frequency of the source is 500 Hz

Maxwell–Vernotte–Cattaneo relaxation times, τ_3 and τ_4. The choice $\tau_4 \geq \tau_3$ gives positive attenuation and increasing τ_4 further enhances the attenuation of the fast wave.

The numerical solver is a direct-grid algorithm based on the Fourier pseudospectral method to compute the spatial derivatives and a Crank–Nicolson time-stepping scheme, which yields the same solutions as the splitting scheme. The simulated snapshots and waveforms illustrate the dissipative and wave-like behavior of the Biot slow and thermal waves at the low and high frequencies, respectively. The differences between the Green–Lindsay and Lord–Shulman
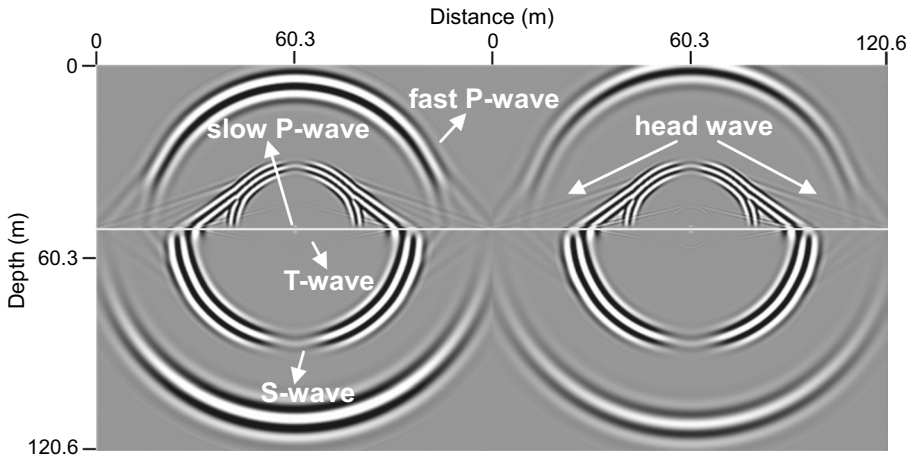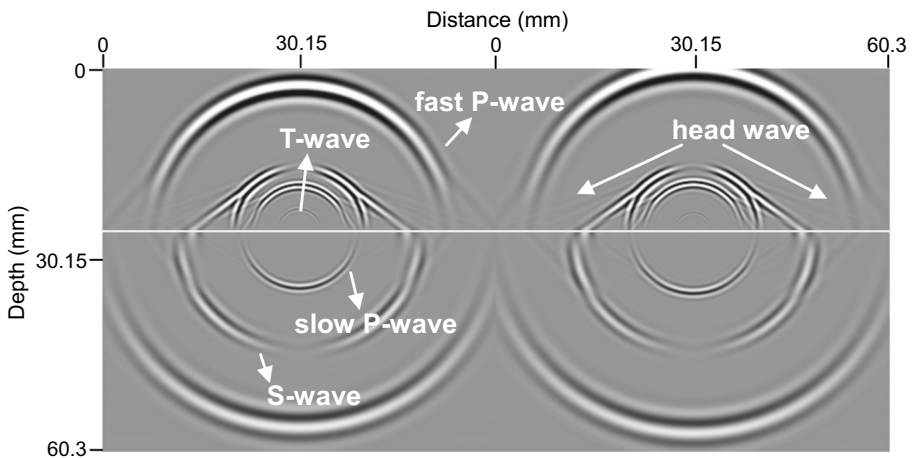

Fig. 23 Snapshots of the v_z component at 9.75 μs, corresponding to the two-layer model based on the LS (left) and GL (right) theories. The interface is located at a depth of 25.5 mm. The differences between the upper and lower media are the values of the dry-rock moduli K_m, μ_m and the bulk specific heat c. The dominant frequency of the source is 1 MHz
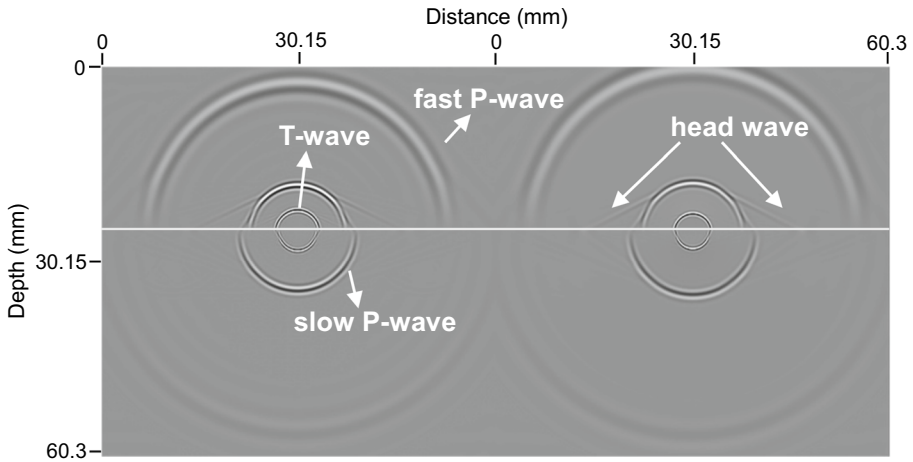
Fig. 24 Snapshots of the *T* component at 9.75 μs, corresponding to Fig. 23. The GL result has been enhanced by a factor 10^4

theories are in agreement with the dispersion analysis. The modeling can be extended to the anisotropic and three-dimensional cases in a future study.

Appendix 1: Plane-wave analysis

We consider a 1D medium to analyze the phase velocity and attenuation of the different waves modes involved in the propagation, because the medium is isotropic. The S wave is not affected by the temperature effects, and its complex velocity is that of Biot theory (Carcione 2014):

$$v_c(\text{ S wave}) = v_c = \sqrt{\frac{\mu}{\rho - \rho_f^2[m - \mathrm{i}\eta/(\omega\kappa)]^{-1}}}. \tag{17}$$

In 1D case, the field vector becomes $\mathbf{v} = [v, q, \sigma, p, T]^\mathsf{T}$. Considering a plane wave of the form $\exp[\mathrm{i}(\omega t - kx)]$, where ω is the angular frequency and k is the complex wavenumber, Eqs. (1), (3) and (5) in 1D case reduce to

$$
\begin{aligned}
&-k\sigma = \omega\rho v + \omega\rho_f q, \\
&kp = \omega\rho_f v + \omega m q - (i\eta/\kappa)q, \\
&\omega\sigma = -kEv - \alpha kM(\alpha v + q) - \omega\beta\bar{\tau}_1 T, \\
&\phi\omega p = \phi kM(\alpha v + q) + \omega\beta_f\bar{\tau}_2 T, \\
&ikT_0\beta\bar{\tau}_4(v + q) = [\gamma k^2 + i\omega c\bar{\tau}_3]T, \\
&\bar{\tau}_l = 1 + i\omega\tau_l, \quad l = 1, \ldots, 4,
\end{aligned}
\tag{18}
$$

where $E = \lambda + 2\mu$.

This is a homogeneous system of linear equations whose solution is not zero if the determinant of matrix **A** is zero, whose components are

$$
\begin{aligned}
&a_{11} = \omega\rho, \quad a_{12} = \omega\rho_f, \quad a_{13} = k, \quad a_{14} = 0, \quad a_{15} = 0, \\
&a_{21} = \omega\rho_f, \quad a_{22} = \omega m - i\eta/\kappa, \quad a_{23} = 0, \quad a_{24} = -k, \quad a_{25} = 0, \\
&a_{31} = -k(E + \alpha^2 M), \quad a_{32} = -\alpha kM, \quad a_{33} = -\omega, \quad a_{34} = 0, \quad a_{35} = -\omega\beta\bar{\tau}_1, \\
&a_{41} = \phi\alpha kM, \quad a_{42} = \phi kM, \quad a_{43} = 0, \quad a_{44} = -\omega\phi, \quad a_{45} = \omega\beta_f\bar{\tau}_2, \\
&a_{51} = -ikT_0\beta\bar{\tau}_4, \quad a_{52} = a_{51}, \quad a_{53} = 0, \quad a_{54} = 0, \quad a_{55} = i\omega c\bar{\tau}_3 + \gamma k^2.
\end{aligned}
\tag{19}
$$

Based on it, we obtain the dispersion relation for P waves:

$$
a_6 v_c^6 + a_4 v_c^4 + a_2 v_c^2 + a_0 = 0,
\tag{20}
$$

where

$$
\begin{aligned}
a_0 &= i\omega^2\phi\gamma ME, \\
a_2 &= -\omega\big\{\phi\big[b\gamma E_G + i\omega\gamma(mE_G + M(\rho - 2\alpha\rho_f)) + cME\bar{\tau}_3\big] \\
&\quad + \beta T_0\bar{\tau}_4\big[\beta_f E\bar{\tau}_2 + (1 - \alpha)M(\phi\beta\bar{\tau}_1 - \alpha\beta_f\bar{\tau}_2)\big]\big\}, \\
a_4 &= b\phi\big[\omega\rho\gamma - icE_G\bar{\tau}_3 - i\beta^2 T_0\bar{\tau}_1\bar{\tau}_4\big] + \omega\Big[i\omega\gamma\phi(m\rho - \rho_f^2) + c\phi\bar{\tau}_3(mE_G \\
&\quad + M(\rho - 2\alpha\rho_f)) + \beta T_0\bar{\tau}_4[\beta\phi(m - \rho_f)\bar{\tau}_1 + \beta_f(\rho - \rho_f)\bar{\tau}_2]\Big], \\
a_6 &= c\phi\bar{\tau}_3\Big[ib\rho + \omega(\rho_f^2 - m\rho)\Big], \\
E_G &= E + \alpha^2 M, \quad b = \frac{\eta}{\kappa}.
\end{aligned}
\tag{21}
$$

When $\beta = \beta_f = 0$, we obtain a quadratic equation about v_c, corresponding to Biot velocities for the fast and slow P waves:

$$
(-ib\rho + \omega m\rho - \omega\rho_f^2)v_c^4 + (ibE_G - \omega mE_G - \omega M\rho + 2\omega\alpha M\rho_f)v_c^2 + \omega ME = 0,
\tag{22}
$$

and an additional root:

$$
v_c = \sqrt{\frac{i\omega a^2}{\bar{\tau}_3}}, \quad a = \sqrt{\frac{\gamma}{c}},
\tag{23}
$$

for the decoupled thermal wave, where a is the thermal diffusivity (Carcione et al. 2019a). It is evident that, at low frequencies, this velocity is zero.

The plane-wave analysis performed here is similar to the 1D time-periodic solutions obtained by Ignaczak and Ostoja-Starzewski (2010), whose complex wavenumbers are given by their Eq. (11.1.32), corresponding to the thermal and elastic waves. The phase velocity and attenuation factor can be obtained from the complex velocity as

$$v_p = \left[\text{Re}\left(v_c^{-1}\right)\right]^{-1} \quad \text{and} \quad Q = \frac{\text{Re}(v_c^2)}{\text{Im}(v_c^2)}, \tag{24}$$

respectively (e.g., Carcione 2014).

Appendix 2: Crank–Nicolson explicit scheme

The Crank–Nicolson explicit scheme has been implemented by Carcione and Quiroga-Goode (1995) to solve the equations of poroelasticity and by Carcione et al. (2019b) to solve the thermoelasticity equations. The scheme, applied to the thermo-poroelasticity equations, is

$$
\begin{aligned}
D^{1/2}v_x &= \beta_{11}(\sigma_{xx,x} + \sigma_{xz,z} - f_x)^n - \beta_{12}p_{,x}^n - \frac{\eta}{\kappa}\beta_{12}A^{1/2}q_x = \Pi_x^n, \\
D^{1/2}v_z &= \beta_{11}(\sigma_{xz,x} + \sigma_{zz,z} - f_z)^n - \beta_{12}p_{,z}^n - \frac{\eta}{\kappa}\beta_{12}A^{1/2}q_z = \Pi_z^n, \\
D^{1/2}q_x &= \beta_{21}(\sigma_{xx,x} + \sigma_{xz,z} - f_x)^n - \beta_{22}p_{,x}^n - \frac{\eta}{\kappa}\beta_{22}A^{1/2}q_x = \Omega_x^n, \\
D^{1/2}q_z &= \beta_{21}(\sigma_{xz,x} + \sigma_{zz,z} - f_z)^n - \beta_{22}p_{,z}^n - \frac{\eta}{\kappa}\beta_{22}A^{1/2}q_z = \Omega_z^n, \\
\epsilon_m &= (A^{1/2}v_x)_{,x} + (A^{1/2}v_z)_{,z}, \\
\epsilon_f &= (A^{1/2}q_x)_{,x} + (A^{1/2}q_z)_{,z}, \\
\epsilon &= \alpha\epsilon_m + \epsilon_f, \\
\dot{\epsilon}_m &= (\Pi_x^n)_{,x} + (\Pi_z^n)_{,z}, \\
\dot{\epsilon}_f &= (\Omega_x^n)_{,x} + (\Omega_z^n)_{,z}, \\
\Delta_\gamma T^n &= c(A^{1/2}\psi + \tau_3 D^{1/2}\psi) + \beta T_0[(\epsilon_m + \tau_4\dot{\epsilon}_m) + (\epsilon_f + \tau_4\dot{\epsilon}_f)] + q^n, \\
T^{n+1} &= T^n + dt\,\psi^{n+1/2}, \\
\Pi^n &= (c\tau_3)^{-1}[\Delta_\gamma T^n - q^n - \beta T_0(\epsilon_m + \tau_4(\Pi_{x,x}^n + \Pi_{z,z}^n) + \epsilon_f + \tau_4(\Omega_{x,x}^n + \Omega_{z,z}^n))] - \frac{1}{\tau_3}A^{1/2}\psi, \\
D^1\sigma_{xx} &= 2\mu(A^{1/2}v_x), x + \lambda\epsilon_m + \alpha M\epsilon - \beta(A^{1/2}\psi + \tau_1\Pi^n) + f_{xx}, \\
D^1\sigma_{zz} &= 2\mu(A^{1/2}v_z), z + \lambda\epsilon_m + \alpha M\epsilon - \beta(A^{1/2}\psi + \tau_1\Pi^n) + f_{zz}, \\
D^1\sigma_{xz} &= \mu[(A^{1/2}v_x), z + (A^{1/2}v_z), x)] + f_{xz}, \\
\phi D^1 p &= -\phi M\epsilon + \beta_f(A^{1/2}\psi + \tau_2\Pi^n) - f_f,
\end{aligned}
\tag{25}
$$

where

$$D^j\phi = \frac{\phi^{n+j} - \phi^{n-j}}{2j dt}, \quad \text{and} \quad A^j\phi = \frac{\phi^{n+j} + \phi^{n-j}}{2}, \tag{26}$$

are the central differences and mean value operators. In this three-level scheme, the particle velocities and ψ at time $(n + 1/2)dt$ and stresses and temperature at time $(n + 1)dt$ are computed explicitly from particle velocities and ψ at time $(n - 1/2)dt$, and stresses and temperature at time $(n - 1)dt$ and ndt, respectively.

For example, by expanding the third equation in (25), we obtain

$$q_x^{n+1/2}\left(1 + \frac{b}{2}\beta_{22}dt\right) = q_x^{n-1/2}\left(1 - \frac{b}{2}\beta_{22}dt\right) + dt[\beta_{21}(\sigma_{xx,x} + \sigma_{xz,z})^n - \beta_{22}p_{,x}^n]. \quad (27)$$

Then,

$$v_x^{n+1/2} = v_x^{n-1/2} + dt\left[\beta_{11}(\sigma_{xx,x} + \sigma_{xz,z})^n - \beta_{12}p_{,x}^n - \beta_{12}\frac{\eta}{2k}(q_x^{n+1/2} + q_x^{n-1/2})\right]. \quad (28)$$

Similarly,

$$\sigma_{zz}^{n+1} = \sigma_{zz}^{n-1} + 2dt\mu(v_z^{n+1/2} + v_z^{n-1/2})_{,z} + 2dt(\lambda + \alpha^2 M)\epsilon_m + 2dt\alpha M\epsilon_f$$
$$- dt\beta(\psi^{n+1/2} + \psi^{n-1/2}) - 2dt\beta\tau_1\Pi^n. \quad (29)$$

The equations for the other components can be similarly derived, based on equation (25). The numerical algorithms can be implemented on a staggered grid. For example, by defining v_x and q_x at coordinate $(x + d_x/2, z)$, v_z and q_z at coordinate $(x, z + d_z/2)$, $\sigma_{xx}, \sigma_{zz}, \psi, T$ and p at $(x + d_x, z + d_z)$, and σ_{xz} at $(x + d_x/2, z + d_z/2)$, the spatial derivatives in equation (25) can be obtained with the pseudospectral method as,

Table 2 Crank–Nicolson scheme for the thermo-poroelasticity equations

Input:

The initialized wavefields, $\sigma_{xx}^{-1}, \sigma_{xx}^0, \sigma_{zz}^{-1}, \sigma_{zz}^0, \sigma_{xz}^{-1}, \sigma_{xz}^0, p^{-1}, p^0, q_x^{-1/2}, q_z^{-1/2},$
$v_x^{-1/2}, v_z^{-1/2}, \psi^{-1/2}, T^0$;

Receiver location (Rx, Rz), time of the recorded snapshot n.

Output:

Simulated wavefields at time slice n, $q_x^{n+1/2}, q_z^{n+1/2}, v_x^{n+1/2}, v_z^{n+1/2}, T^{n+1}$;

Waveforms of v_x, v_z, q_x, q_z and T at Receiver location (Rx, Rz).

1: **for** $t = 0; t \le N; t++$ **do**

2: // update q_x, v_x, q_z, v_z with stresses at time t.

Update $q_x^{t+1/2}$ and $v_x^{t+1/2}$, based on equations (27) and (28);

Update $q_z^{t+1/2}$ and $v_z^{t+1/2}$, in the same manner as equations (27) and (28);

Output $q_x^{n+1/2}, q_z^{n+1/2}, v_x^{n+1/2},$ and $v_z^{n+1/2}$ if $n = t$;

3: // update ψ with particle velocities, at both $t + 1/2$ and $t - 1/2$.

Update $\epsilon_m, \epsilon_f, \dot{\epsilon}_m, \dot{\epsilon}_f$ using equation (25);

Update $\psi^{t+1/2}$, based on equation (10);

4: // update T.

$T^{t+1} = T^t + dt\psi^{t+1/2}$;

Output T^{n+1}, if $n = t$;

5: // update stresses with particle velocities and ψ, at $t + 1/2$ and $t - 1/2$.

Update σ_{zz}^{t+1} using equation (29);

Update $\sigma_{xx}^{t+1}, \sigma_{xz}^{t+1}$ and p^{t+1} similarly;

6: **end for**

7: **return** v_x, v_z, q_x, q_z and T at location (Rx, Rz) for all $t = 0 : N$.

$$
\begin{aligned}
M_{,x} &= \text{IFFT}\Big[\text{FFT}(M)ik_x\exp(ik_xd_x/2)\Big], &\quad M &= \sigma_{xx},\ p,\ v_z, \\
M_{,z} &= \text{IFFT}\Big[\text{FFT}(M)ik_z\exp(ik_zd_z/2)\Big], &\quad M &= \sigma_{zz},\ p,\ v_x, \\
N_{,x} &= \text{IFFT}\Big[\text{FFT}(N)ik_x\exp(-ik_xd_x/2)\Big], &\quad N &= \sigma_{xz},\ v_x,\ q_x, \\
N_{,z} &= \text{IFFT}\Big[\text{FFT}(N)ik_z\exp(-ik_zd_z/2)\Big], &\quad N &= \sigma_{xz},\ v_z,\ q_z, \\
T_{,zz} &= \text{IFFT}\Big[-k_z^2\text{FFT}(T)\Big], \\
T_{,xx} &= \text{IFFT}\Big[-k_x^2\text{FFT}(T)\Big],
\end{aligned}
\tag{30}
$$

where FFT and IFFT are the forward and backward fast Fourier transforms, respectively, and k_x and k_z are the wavenumbers along x and z directions, respectively. A list of the algorithm in pseudo-code form is given in Table 2.

The stability analysis for similar equations has been studied in Carcione and Quiroga-Goode (1995), with a Von Neumann stability analysis based on the eigenvalues of the amplification matrix. The algorithm has first-order accuracy but possesses the stability properties of implicit algorithms and the solution can be obtained explicitly. Alternatively, implicit methods can also be used when the differential equations are stiff, but are more cumbersome to implement than explicit methods. The instability is mainly due to the presence of the quasi-static mode (the Biot slow wave). While the eigenvalues of the fast waves have a small real part, the eigenvalue of the Biot wave (in the quasi-static regime) has a large real part. Indeed, the simple explicit first-order accurate Crank–Nicolson scheme proposed here provides an efficient scheme to deal with the stiffness, as shown in Carcione and Quiroga-Goode (1995).

References

Armstrong BH (1984) Models for thermoelastic in heterogeneous solids attenuation of waves. Geophysics 49:1032–1040

Bear J, Sorek S, Ben-Dor G, Mazor G (1992) Displacement waves in saturated thermoelastic porous media, I Basic equations. Fluid Dyn Res 9(4):155–164

Berezovski A, Maugin GA (2001) Simulation of thermoelastic wave propagation by means of a composite wave-propagation algorithm. J Comput Phys 168(1):249–264

Berryman JG (1981) Elastic wave propagation in fluid saturated porous media. J Acoust Soc Am 69(2):416–424

Biot MA (1956) Thermoelasticity and irreversible thermodynamics. J Appl Phys 27(3):240–253

Biot MA (1962) Mechanics of deformation and acoustic propagation in porous media. J Appl Phys 33(4):1482–1498

Budiansky B, Sumner EE Jr, OĆonnell RJ (1983) Bulk thermoelastic attenuation of composite materials. J Geophys Res Solid Earth 88(B12):10343–10348

Carcione JM (2014) Wave Fields in real media. Theory and numerical simulation of wave propagation in anisotropic, anelastic, porous and electromagnetic media. Elsevier, Amsterdam

Carcione JM, Cavallini F, Wang E, Ba J, Fu L (2019a) Physics and simulation of wave propagation in linear thermo-poroelastic media. J Geophys Res Solid Earth 124(8):8147–8166

Carcione JM, Gei D, Santos JE, Fu L, Ba J (2020) Canonical analytical solutions of wave-induced thermoelastic attenuation. Geophys J Int 221(2):835–842

Carcione JM, Quiroga-Goode G (1995) Some aspects of the physics and numerical modeling of Biot compressional waves. J Comput Acoust 3(04):261–280

Carcione JM, Wang Z, Ling W, Salusti E, Ba J, Fu L (2019b) Simulation of wave propagation in linear thermoelastic media. Geophysics 84(1):T1–T11

Dhaliwal RS, Sherief HH (1980) Generalized thermoelasticity for anisotropic media. Q Appl Math 38(1):1–8

Green AE, Lindsay KE (1972) Thermoelasticity. J Elast 2(1):1–7

Gurevich B, Kelder O, Smeulders DMJ (1999) Validation of the slow compressional wave in porous media: Comparison of experiments and numerical simulations. Transp Porous Media 36(2):149–160

Hetnarski RB, Ignaczak J (1999) Generalized thermoelasticity. J Therm Stresses 22(4–5):451–476

Ignaczak J, Ostoja-Starzewski M (2010) Thermoelasticity with finite wave speeds. Oxford University Press, Oxford

Jacquey AB, Cacace M, Blöcher G, Scheck-Wenderoth M (2015) Numerical investigation of thermoelastic effects on fault slip tendency during injection and production of geothermal fluids. Energy Procedia 76:311–320

Kelder O, Smeulders DMJ (1997) Observations of the Biot slow wave in water saturated Nivelsteiner sandstone. Geophysics 62(6):1794–1796

Norris A (1992) On the correspondence between poroelasticity and thermoelasticity. J Appl Phys 71(3):1138–1141

Lord H, Shulman Y (1967) A generalized dynamical theory of thermoelasticity. J Mech Phys Solids 15(5):299–309

Poletto F, Farina B, Carcione JM (2018) Sensitivity of seismic properties to temperature variations in a geothermal reservoir. Geothermics 76:149–163

Rawal C, Ghassemi A (2014) A reactive thermo-poroelastic analysis of water injection into an enhanced geothermal reservoir. Geothermics 50:10–23

Rudgers AJ (1990) Analysis of thermoacoustic wave propagation in elastic media. J Acoust Soc Am 88(2):1078–1094

Sharma MD (2008) Wave propagation in thermoelastic saturated porous medium. J Earth Syst Sci 117(6):951–958

Singh B (2011) On propagation of plane waves in generalized porothermoelasticity. Bull Seismol Soc Am 101(2):756–762

Wang Z, Fu L, Wei J, Hou W, Ba J, Carcione JM (2020) On the Green function of the Lord-Shulman thermoelasticity equations. Geophys J Int 220(1):393–403

Youssef HM (2007) Theory of generalized porothermoelasticity. Int J Rock Mech Min Sci 44(2):222–227